

Nanoscale and Microscale Thermophysical Engineering



ISSN: 1556-7265 (Print) 1556-7273 (Online) Journal homepage: https://www.tandfonline.com/loi/umte20

Bio-Inspired Stretchable Selective Emitters Based on Corrugated Nickel for Personal Thermal Management

Martí Sala-Casanovas, Anirudh Krishna, Ziqi Yu & Jaeho Lee

To cite this article: Martí Sala-Casanovas, Anirudh Krishna, Ziqi Yu & Jaeho Lee (2019) Bio-Inspired Stretchable Selective Emitters Based on Corrugated Nickel for Personal Thermal Management, Nanoscale and Microscale Thermophysical Engineering, 23:3, 173-187, DOI: 10.1080/15567265.2019.1586017

To link to this article: https://doi.org/10.1080/15567265.2019.1586017

+	View supplementary material 🗹
	Published online: 14 Mar 2019.
	Submit your article to this journal 🗗
ılıl	Article views: 336
CrossMark	View Crossmark data 🗗
4	Citing articles: 1 View citing articles 🗹





Bio-Inspired Stretchable Selective Emitters Based on Corrugated **Nickel for Personal Thermal Management**

Martí Sala-Casanovas 6, Anirudh Krishna 6, Zigi Yu 6, and Jaeho Lee 6

Department of Mechanical and Aerospace Engineering, University of California, Irvine, CA, USA

ABSTRACT

While dynamic photonic materials have attracted much attention and there are well-known examples of color-changing species in nature, dynamic thermal control via modulation of optical properties has made relatively little progress. By replicating unique properties of desert ants and chameleons, here we present a stretchable selective emitter based on corrugated nickel that can modulate the emissivity to provide dynamic thermal control on human bodies. By evaporating nickel on a pre-strained polymer, we create 700-nm periodic corrugations that increase the nickel absorptivity from 0.3 to 0.7 in 0.2–2.5 µm wavelengths due to multiple scattering, as supported by spectroscopy and computations. The optical change is reversible and accompanies ambient surface temperature variations in 305-315 K. We demonstrate a wearable system, and the corrugated nickel on a human body at 309 K allows a heat flux of 62 Wm⁻² out of the skin when stretched and 79 Wm⁻² into the skin when released.

ARTICLE HISTORY

Received 13 November 2018 Accepted 15 February 2019

KEYWORDS

Wearable device; selective absorber; dynamic thermal control; thermoregulation

From stained-glass windows [1] of medieval times to dynamic displays [2] of today, the need to control optical properties of materials has a long history. Recent studies in photonic materials have shown important advances in interactive optical devices [3] and dynamic structural coloration [4,5]. However, the dynamic control of optical properties such as reflectivity is not new in nature. The well-known physiological color change in chameleons [6], squids [7] and flatfishes [8], the structural dynamic coloration of beetles [9], and the specialized abdominal scales that function as diffraction grating structures in rainbow peacock spiders [10], highlight the importance of nanophotonics in optical control [11]. Emulating the success of the natural photonic structures, biomimetic structures [12,13] aim to control the optical properties of materials in the visible wavelengths (400-700 nm) of the electromagnetic spectrum. While the dynamic coloration or optical variations is important for communication in the biological world [14], and has led to the development of bio-inspired optical devices, thermal control based on evolutionary adaptations of extreme-environment species such as Saharan silver ants [15] is yet to exploited for practical applications.

Thermal management in the ambient environment demands spectral control of optical properties. While the incoming solar irradiation [16] heats up surface areas in the wavelength range of 200-2500 nm [17], the atmospheric transmission window [18] allows re-emission of the absorbed heat (i.e. cooling) from ambient surfaces to outer space in the mid-infrared (mid-IR) wavelength range of 8-14 µm [19-23]. Because of the distinct spectral ranges allowed for heating and cooling, conventional approaches relying on a high- or low-emissivity material do not offer optimal solutions. We thus rely on engineered surfaces that can be designed to suit a specific application by varying the emissivity along specific regions of the

Irvine, CA 92697, USA



CONTACT Jaeho Lee 🔯 jaeholee@uci.edu 🗈 Department of Mechanical and Aerospace Engineering, University of California,

*These authors contributed equally to this work.

Color versions of one or more of the figures in the article can be found online at www.tandfonline.com/umte.

Supplemental data for this article can be accessed here

electromagnetic spectrum. By using selective emitters to tailor the emissivity spectrum according to our needs, we can regulate thermal exchanges and optimally control the temperature without using electricity or bulky heat exchangers. The radiative thermal control by selective emitters is attractive for different systems such as solar absorbers [24], thermal imaging devices [25], and bolometers [26]. Rapid developments in selective emitters based on passive nanophotonic structures [20,23,27], also show promise for personal- to system-level thermal control [28,29].

The advancements in personal thermal management have mirrored the emergence and growth of the field of wearables. With the rise of personal health monitors [30], wearable radio-frequency antennas [31], and wearable electrochromic displays [32], there is an increased need for flexible and wearable thermal management solutions [33]. This has so far been realized using selective emitters based on flexible substrates, examples are blended textiles [34], nano-polyethylene fabrics [17,35,36], and nanowire-enhanced textiles [27]. However, most state-of-the-art selective emitter systems [19-21,37] lack dynamic control capabilities. The passive systems are unable to address diurnal or seasonal changes in thermal environments, and this lack of dynamic control affects the scope of their applications. The limitations of dynamic control of radiative and optical properties can be addressed in part by phase-change materials (PCMs) [38,39]. However, the use of PCMs heavily relies on the phase transition temperature, which might not lie in the favorable range of operation for the desired solution.

To overcome the dependence on transition temperature, we look for bio-inspired IR thermal solutions. A prominent example is the radiative cooling abilities of the Saharan silver ant [15]. The remarkable cooling capability of the Saharan silver ants is attributed to their structural features, in which a dense array of hairs is characterized by triangular cross-sections. The hair structures on the ant's surface are reflective in the solar spectrum and highly emissive in the mid-IR range, which help them stay cool even in extremely hot temperature conditions of the desert [15]. We also find inspiration from chameleons. The ability of chameleons to shift their appearance to communicate with others is a well-documented phenomenon [6]. The color-shift is achieved by means of strain-dependent variations in the distance between photonic nanocrystals and the accompanying spectral shift in reflectivity values. Here we aim to integrate the thermal radiation control mechanism offered by the ants with the dynamic control mechanism offered by chameleons [6] and to provide dynamic radiative thermal radiation control.

We emulate the spectral variations in emissivity based on the unique morphology of the anthair structures with periodic triangular crests and troughs yielding a corrugated surface morphology. We use corrugated nickel to achieve effective modulation in surface emissivity. Nickel is ideal for thermal control on human bodies in the range between 305-314 K because of its relatively high absorptivity values (>0.3) in the solar spectrum (0.2-2.5 μm wavelengths), as compared to conventional metals for fabrication of selective emitters as gold [40], silver [41], or platinum [42] (which display a solar absorption coefficient <0.2) [43]. The high solar spectrum emissivity combined with a low mid-IR emissivity (as opposed to highly emissive ceramics) makes nickel a good candidate for tunable emissivity control for solar absorption and personal thermal management solutions. While other metals such as molybdenum possess comparably high solar absorptivity values (around 0.4) [44], nickel is chosen due to ease of fabrication and low cost, and its use in existing solar absorber applications [45].

The dynamic modification of optical properties is achieved by emulating the strain-dependent optical control mechanism in chameleons. Other examples include deformation-controlled mechanochromic devices [46], switchable transparency windows [47,48], and adaptive IR-reflecting solutions [49]. We integrate the corrugated nickel with a stretchable elastomeric substrate (3M VHB 4910), in which the strain-induced corrugations lead to dynamic control of optical properties. The bio-inspired corrugated nickel thin film combines unique thermal and optical properties of desert ants [15] and chameleons [6] (Figure 1). The results presented in this work pave innovative ways of thermal radiation control that utilize stretchable selective emitters.

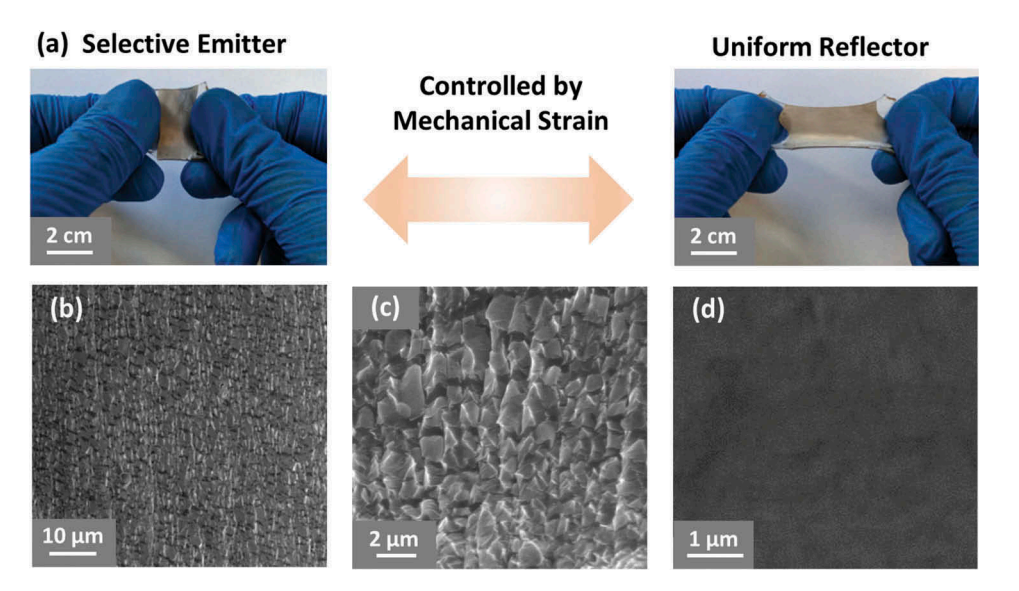


Figure 1. Bio-inspired stretchable selective emitter design. (a) Our work develops selective emitters based on corrugated nickel that resemble the morphology of desert ants and develops a dynamic system based on a stretchable polymer that resembles the color change mechanism of chameleons. The corrugated nickel films can selectively transform from non-emissive to emissive surfaces. (b) The SEM images show a 10 nm thick nickel layer on a stretchable substrate and sub-micron scale (0.6–0.8 µm) surface corrugation features spanning uniformly over a large area (> 1 cm²). (c) Angled SEM image shows the corrugated nickel surface has a triangular corrugation profile, which is also confirmed by AFM analysis (Figure S4). (d) The far-right image shows a flat nickel sample.

Results

Computational predictions of optical properties

This work computes the spectral optical properties of corrugated nickel, including reflectivity, transmissivity, and consequently emissivity, using the rigorous couple wave analysis (RCWA) [50,51] and finite-difference time-domain (FDTD) [52] methods (Figure 2). The RCWA method considers topographical variations and handles rigorous solutions of Maxwell's equations [23,53]. Direct results from RCWA yield scattering matrices in the forward and reverse directions, from which reflectivity (ρ) and transmissivity (τ) are computed. The emissivity is assumed identical to the absorptivity by Kirchhoff's law [54] and is computed from the reflectivity and transmissivity ($\alpha = 1-\rho-\tau$) [54]. The FDTD method discretizes the samples and solves for space- and time-variant Maxwell's equation for each unit cell. RCWA is semi-analytical and treats the waves and fields as sets of gratings, hence making it very effective for corrugated structures. On the other hand, FDTD is superior in modeling curved surfaces and spherical shapes in full three-dimension. While FDTD is time-consuming, RCWA is more efficient towards optimizing the designs by variation of geometrical parameters.

In the work presented here, the corrugated nickel structures are modelled as a periodic array of triangles that are approximated using a staircase pattern composed of 30 steps, found to be a good approximation after a convergence analysis (Figure S1). This value not only offers sufficient accuracy but also makes the computational load manageable. The optical properties such as spectral permittivity and complex refractive index of the nickel layer [55–57] and the elastomer substrate [58–60] are taken from literature and considered as input parameters in the computations. The geometrical variables that act as parameters controlling the topography of the corrugated nickel structures include the metallic layer thickness and the corrugated pitch. The computational parameters, i.e. nickel layer thickness and corrugation pitch, are then optimized to provide maximum solar absorption. The thickness and pitch are inter-dependent parameters due to fabrication constraints. The layer thickness is taken to be 10 nm

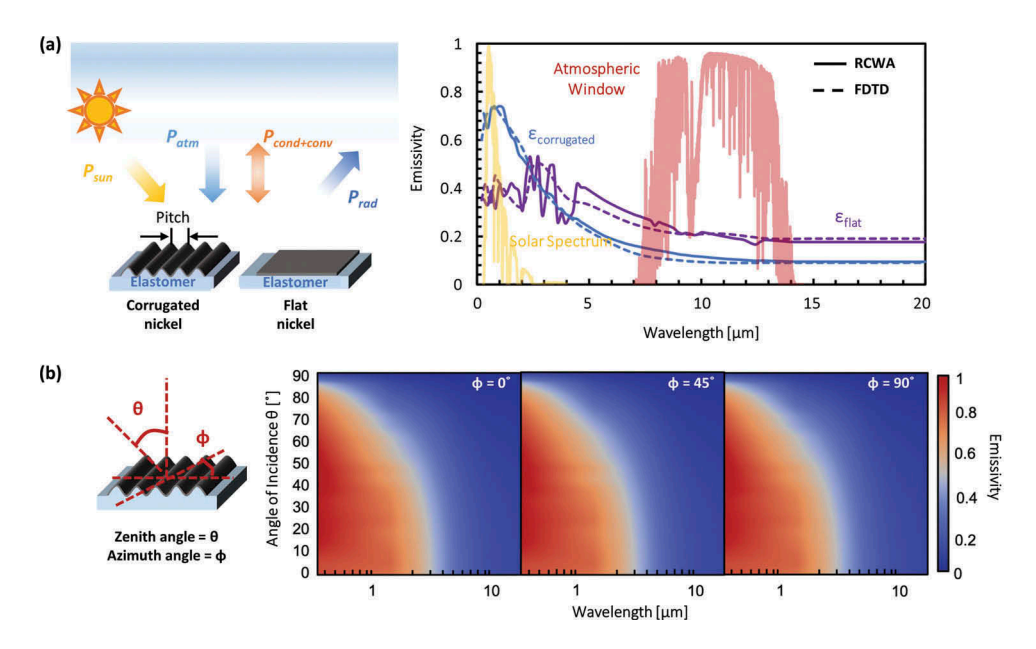


Figure 2. Computations by RCWA and FDTD methods. (a) The computational data for corrugated nickel of 700 nm pitch and flat nickel, both on elastomer substrate, are shown. The unit cell is replicated using periodic boundary conditions. Perfectly matched layer boundary conditions are applied at the bottom and top surfaces to avoid any undesired reflection of the plane wave at the physical boundaries. While the flat nickel shows an emissivity starting off at 0.4, reaching a value of 0.2 in the IR, the corrugated nickel displays a higher emissivity in the visible to near-IR, at 0.7, going down to 0.1 in the mid-IR. This elevated emissivity is attributed to multiple internal reflections of incident radiation, leading to a reduction in transmissivity and a consequent increase in emissivity. The left side schematic depicts the thermal interactions of the samples with the ambient environment. (b) The angle-dependent emissivity profile for the corrugated nickel samples, computed using the RCWA method. Varying the angle of incidence (zenith angle) from normal to 0° incidence, we notice a largely invariant emissivity profile, up to an angle of around 75°. The emissivity profile also remains predominantly unchanged for various azimuth angles as well. The largely invariant emissivity profile allows for the application of the corrugated nickel samples in wide fields of use. (Figure S2).

for the computation, on top of a substrate of 3M VHB 4910 elastomer, while the corrugated pitch is taken to be 700 nm between each successive topographic crest. The results depict substantial variations in the visible to near-IR emissivity values of corrugated and flat nickel (Figure 2). While the flat nickel maintains an emissivity of 0.3–0.4 within the wavelengths of 200 nm to 2 μ m, the corrugated nickel attains an emissivity of 0.7 within the same spectral range. We attribute this increase in emissivity to interference among adjacent topographic ridges of corrugated nickel. The accompanying phenomena of multiple internal reflections significantly reduce the transmissivity through the sample, thereby increasing the emissivity.

The general emissivity trend is also captured by the Sparrow model [61], which predicts the overall surface emissivity for varying apex angles for surface corrugations or V-grooves. The Sparrow model shows a general increase in emissivity with corrugation of the surface (an average of 0.70 for corrugated, as opposed to an average of 0.36 for simple, flat surfaces). The increase in emissivity in the Sparrow model is due to the increase in internal reflection between adjacent grooves/corrugations [61]. The increased internal reflection phenomena lead to an overall drop in transmissivity. With the reflectivity remaining fairly unaffected, the drop in transmissivity leads to an increase in emissivity. While this may provide a general idea of the trend of emissivity variations with increased or decreased corrugation angles, it fails to capture the more intricate topographical variations or spectral results that can be resolved with the RCWA or FDTD computations.

The angle- dependency in the emissivity of the sample (Figure 2b) is also studied to ensure optimal performance for a wide range of angles of incidence (Figure S2). The results demonstrate



no noticeable change in the spectral emissivity of the corrugated nickel samples for angles of incidence up to 75°, with no variation with respect to azimuth orientation. The negligible variation in emissivity behavior allows for the use of the corrugated nickel samples in varying geographic latitudes or daylight hours with minimal deviation from expected radiative performance.

Experimental characterization of optical properties

The corrugated and flat nickel samples are fabricated by electron beam evaporation of 10 nm of nickel on the elastomer substrate. The fabricated corrugated nickel samples show a pitch of 600-800 nm for a pre-strain value centered around 250%, as has been verified by the SEM images (Figure S3). The triangular surface morphology has also been verified by AFM analysis (Figure S4) and angled SEM imaging (Figure 1, Figure S5), validating the use of triangular corrugations for computational modeling. Flat nickel samples were also prepared during the same deposition run on an un-stretched flat substrate, and both samples are characterized by reflectance spectroscopy in the wavelength range of 200 and 2500 nm.

The optical data for flat and corrugated nickel films show a significant difference in the visible spectrum (Figure 3). As predicted by computational results (Figure 2a), the corrugated nickel film shows high emissivity values (>0.6) in the visible to near-IR ranges (200-2500 nm wavelengths) compared to the flat nickel film (with an emissivity <0.4). We performed measurements of corrugated nickel by stretching and releasing the elastomer and demonstrated reconfigurable emissivity variations, which can be utilized for dynamic thermal control. The corrugated nickel undergoes a strain of 200%, attaining an emissivity of 0.4. The emissivity profile of the stretched nickel is nearly the same as the emissivity profile offered by flat nickel (Figure 3c), thereby facilitating dynamic mechanically-induced control of spectral emissivity.

With respect to the emissivity in the mid-IR region, the results deviate from what was ideally expected by computation. This is attributed to the presence of cracks perpendicular to the corrugated lines direction. Due to the large pre-strain applied before the evaporation process, when the sample is released the deformation in the transversal direction exceeds the maximum plastic strain of nickel. Therefore, the nickel appears to be fragmented in SEM images (Figure S3). This phenomenon is considered in the thermal performance computations by creating a modified RCWA model in which the unit cell is not completely coated with nickel, resembling the actual structure (Figure S11). In order to validate this model experimentally, we measured the mid-IR emissivity values (between the wavelengths of 7.5-14 μm) using IR thermography. The results depict a spectral average mid-IR emissivity of 0.82 for the flat nickel, with a value of 0.85 recorded for the corrugated nickel. The lack of noticeable variation in the mid-IR emissivity, corroborated by RCWA computations, directs the attention to the solar spectrum data instead.

Thermal performance and predictions

The tunable emissivity modulated by mechanical control in corrugated nickel enables novel dynamic temperature control systems. To predict the impact of corrugated nickel surfaces in normal ambient conditions, considerable heat transfer by convection and conduction (i.e. $h_c = 12 \text{ Wm}^{-2}\text{K}^{-1}$) are assumed with transient solar irradiance in the clear sky [23]. We take the ambient conditions to be average values for California, with the ambient temperature varying between 286 K and 300 K through the day. The solar azimuth angle of incidence is also assumed to be the value taken at California, with the average angle being 30°. The thermal performance of the selective emitters is then characterized by the thermal energy balance on their surface (Equation S1). The model predicts the corrugated nickel film to offer the steady-state temperature of 310-315 K in the case of normal ambient conditions with a gentle breeze ($h_c = 12 \text{ Wm}^{-2} \text{K}^{-1}$) (Figure 4). The surface temperature is higher than that of ambient air due to increased absorption of incident solar radiation. This is

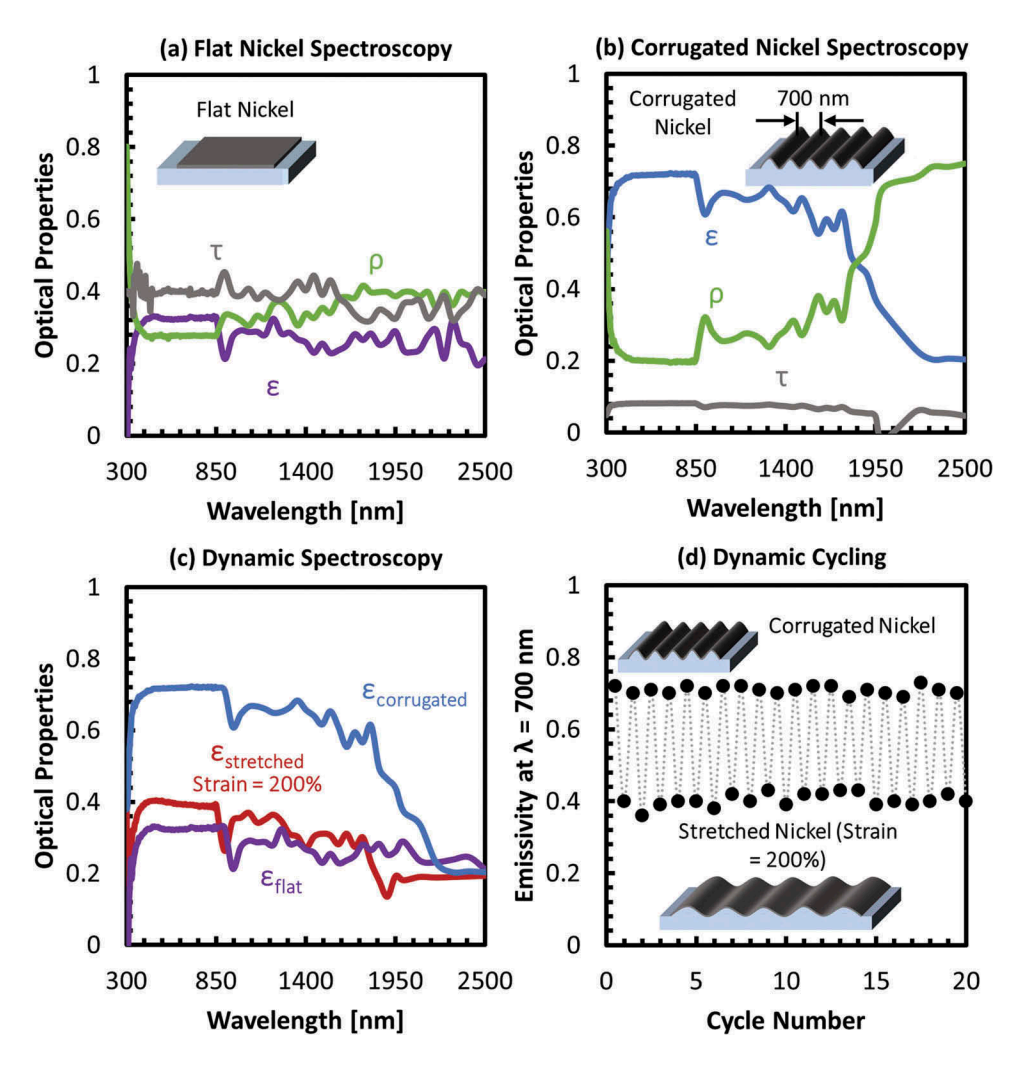
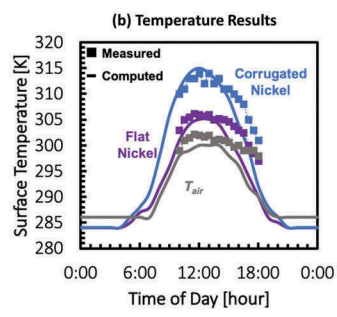


Figure 3. Reflectance spectroscopy data. The flat nickel sample includes a 10 nm thick film of nickel on a stretchable elastomer substrate, and the emissivity (ϵ) spectrum has been obtained by measuring the reflection (ρ) and transmission (τ) data. Compared to the flat film (a), the emissivity in the corrugated film (b) increases due to multiple scattering events and increased absorption. By varying the corrugation via mechanical straining, the emissivity can be dynamically controlled. (c) The corrugated nickel system demonstrates the emissivity control from 0.7 to 0.4 in the visible spectrum, which leads to significant changes in solar absorption and radiative heating properties. The original sample length is 25 mm. (d) The data also show that the fully stretched corrugated sample restores the emissivity and optical properties of the flat samples and is repeatable up to 20 cycles of stretching and releasing the samples. At a wavelength of 700 nm the relaxed samples show an emissivity of 0.7, whereas the stretched samples show an emissivity of 0.4.

contrasted with flat nickel, which heats up to 3 K above the ambient air due to a lower solar absorptivity.

The predicted tunable temperature range is shown to be 10–12 K in the normal ambient conditions. During the day, around 12 noon, the temperature reaches 310-315 K for the relaxed corrugated nickel due to substantial solar irradiation, but the temperature of the flat and stretched corrugated nickel stays at 303-305 K. The corrugated samples are also made to undergo repeated cycles of stretching and relaxation with strains up to 200%. The results demonstrate a cyclical control of surface temperature varying from 312-314 K for the relaxed corrugated nickel to 304-306 K for the stretched state, depicting a simple mechanical actuation on the corrugated nickel leading to a substantial difference





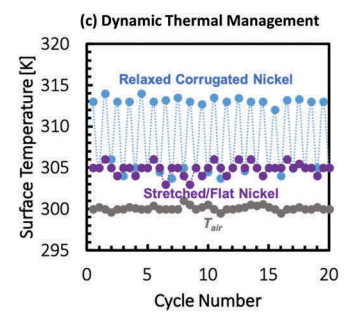


Figure 4. (a) Thermal characterization of stretchable selective emitters using outdoor temperature measurements. The samples were placed in a mechanical holder facilitating stretching, which was then placed resting on thermal isolation legs. (b) The temperature predictions and thermocouple measurement of corrugated and flat nickel samples under ambient conditions showing a temperature difference of 10–12 K between the flat and corrugated samples. (c) The temperature difference between the flat and corrugated designs promises dynamic controllability, as demonstrated by the cyclic measurements of stretching and relaxation. The measurements were taken at 12 noon and tested under 20 cycles of stretching to a strain of 200% and relaxation, indicating a reduction in heating upon stretching the sample, caused by morphology change in the corrugated nickel.

in ambient thermal performance. The corrugated samples have been characterized by IR thermography on a temperature-controlled hot plate for the average emissivity measurement. Based on the emissivity data, the surface temperature has been measured using thermography on a rooftop experimental stage that is exposed to the ambient environment (Figure 4). The corrugated samples tested systematically using a mechanical holder demonstrate reconfigurable emission and thermal properties throughout the day in the ambient environment.

Based on the corrugation effect, the nickel surface can provide a stable temperature throughout the day for potential applications in wearable electronics or comfort clothing. A preliminary demonstration of the use of corrugated nickel samples in personal applications has been done through measuring the temperature change when stretching the corrugated nickel samples on top of the human body. The corrugated nickel samples were strapped to the chest and to the wrist to evaluate the strain/flexing-controlled temperature and heat flux changes. While the on-chest samples required manual straining and fastening, the on-wrist samples were strained by the flexion and extension movement of the human wrist. The samples were then characterized by IR thermography under identical measuring conditions on the same day. The skin temperatures on the chest and wrist were measured using thermocouples to avoid uncertainty in the skin emissivity input parameter for IR thermography. While the body temperature depends on individual conditions, i.e. gender, body mass index, and ethnical origin [62], there are clear differences between different skin zones [63]. In our study, the chest depicted a temperature of around 309 K, while the wrists depicted temperatures of around 305 K. The chest can be assumed to be thermally analogous to the forehead, due to the similar temperature values on both locations [62]. The temperature in the relaxed and stretched states of the corrugated nickel samples on the chest were measured to be 309.7 K and 308.8 K, while on the wrist, they were measured to be 307.0 K and 305.1 K (Figure 5). While ideally the samples are assumed to be in perfect contact with the human body, real life measurements might not allow it, resulting in slight variations between measured and computed values of temperature.

The recorded surface temperatures can then be translated into estimates for the conduction heat flux into/drawn away from the human skin $(P_{cond}^{"})$. The $P_{cond}^{"}$ values are then determined by a one-dimensional approximation for the heat conduction equation, giving $P''_{cond} = \frac{\Delta T}{R''_{th}}$, where ΔT is the difference in temperature between the skin and the surface of the corrugated nickel, and the thermal conductive resistance is given by $R''_{th} = \frac{L}{k}$. Here, L is the thickness of the sample (1 mm for relaxed state and 0.45 mm for stretched state), with k being the thermal conductivity of the sample substrate, taken to be 0.16 Wm⁻¹K⁻¹ [60]. For measurements on the chest, the ΔT for the samples is 0.7 K while relaxed and

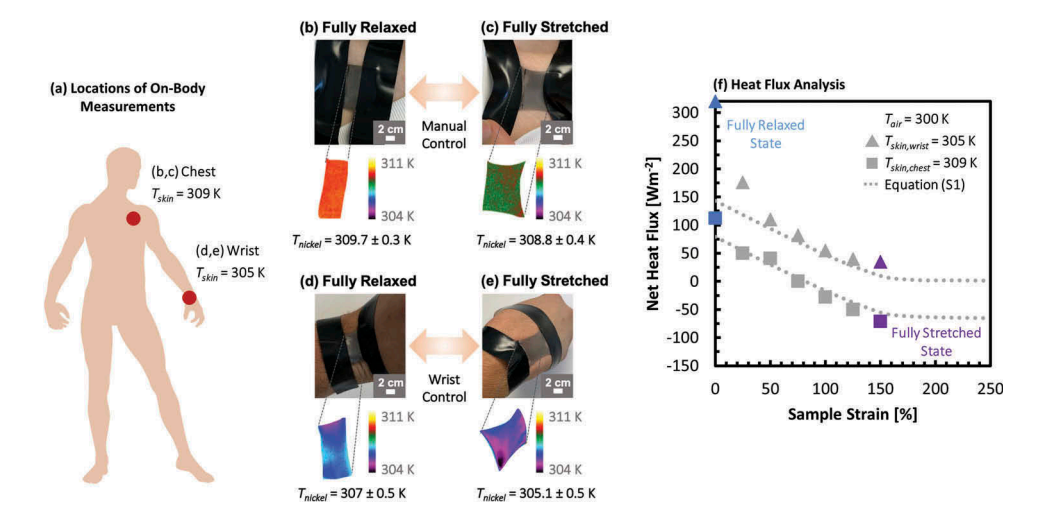


Figure 5. (a) Demonstration of the corrugated nickel samples as a wearable system on different locations of the human body. We perform temperature and heat flux measurements by placing the sample on the chest (b, c) (where the skin temperature is 309 K) and wrist (d, e) (where the skin temperature is 305 K). The chest is assumed equivalent to the forehead due to the similar skin temperature on both locations. The IR imaging (insets) depicts a measurement of temperatures for the nickel samples. On the chest, the relaxed nickel (b) shows a temperature of 309.7 ± 0.3 K, and the stretched nickel (c) shows a surface temperature of 308.8 ± 0.4 K. On the wrist, the relaxed nickel (d) shows a temperature of 307.0 ± 0.5 K, and the stretched nickel (e) shows a surface temperature of 305.1 ± 0.5 K. (f) The net heat flux into or out of the human body at 309 K (chest) and 305 K (wrist) in ideal contact with the corrugated nickel samples. The theoretical prediction for the heat flux based on Equation S1 is shown by a dotted line. While the on-chest samples (squares) depict heating to cooling from 79.2 Wm $^{-2}$ to -62.5 Wm $^{-2}$, the on-wrist samples (triangles) only depict heating from 142.9 Wm $^{-2}$ to 1.4 Wm $^{-2}$.

-0.2 K while stretched, giving P_{cond} values of 112.0 Wm⁻² into the skin while relaxed and -71.1 Wm⁻² out of the skin while stretched. For measurements on the wrist, the ΔT for the samples is 2.0 K while relaxed and 0.1 K while stretched, giving P_{cond} values of 320.0 Wm⁻² into the skin while relaxed and 35.6 Wm⁻² into the skin while stretched.

The values of heat flux in or out of the human body depend on the skin temperature, which varies from one location to another. When the sample is located on top of the human chest, the calculations [20,23], at 12 noon with a convective coefficient of $12 \text{ Wm}^{-2}\text{K}^{-1}$ and an incoming solar radiation of 529 Wm^{-2} show a net heat flux (P_{net} = P_{sun} - P_{rad} + P_{atm} + P_{conv}) of -62.5 Wm^{-2} of heat drawn from the skin while stretched (with P_{sun} = 198.7 Wm^{-2} , P_{rad} = 399.4 Wm^{-2} , P_{atm} = 244.1 Wm^{-2} , P_{conv} = -105.9 Wm^{-2}), and 79.2 Wm^{-2} of heat going into the skin while relaxed (with P_{sun} = 379.5 Wm^{-2} , P_{rad} = 456.0 Wm^{-2} , P_{atm} = 269.6 Wm^{-2} , P_{conv} = -113.9 Wm^{-2}) (Supplementary Information Section S6). The calculations agree well with the values obtained with IR camera measurements on the chest (Figure 5). The measurements were done with the corrugated nickel sample fastened to the chest and manually stretched in steps to a maximum strain of 150%. The on-chest measurements depict net heat flux to the human body varying from net positive (into the body) to net negative (out of the body). However, the level of strains that enable these changes cannot be achieved by the natural flexing of the human chest. The flexion/extension-enabled strain variations can be achieved by fastening the corrugated nickel samples to the wrist.

For applications on the wrist, where the skin temperature is 305 K, the net heat flux is positive into the skin for both stretched and relaxed (varying from near-zero to largely positive). Repeating the calculation at 12 noon with a convective coefficient of 12 Wm⁻²K⁻¹, the heat fluxes are estimated as P_{net} of 1.4 Wm⁻² of heat going into the skin while stretched (with P_{sun} = 198.7 Wm⁻², P_{rad} = 381.3 Wm⁻², P_{atm} = 244.1 Wm⁻², P_{conv} = -60.1 Wm⁻²) and 142.9 Wm⁻² of heat going into the skin while relaxed (with P_{sun} = 379.4 Wm⁻², P_{rad} = 435.4 Wm⁻², P_{atm} = 269.6 Wm⁻², P_{conv} = -70.7 Wm⁻²). This human actuation-induced control over emissivity and consequently temperature of the samples acts as a proof-



of-concept for applications of the corrugated nickel structures in the fields of personal thermal management and wearable electronics (Figure 5).

We observe that for a low skin temperature of 305 K on the wrist, the device only provides heat to the body $(P_{net}^{"} = 142.9 \text{ Wm}^{-2} \text{ when relaxed and } P_{net}^{"} = 1.4 \text{ Wm}^{-2} \text{ when stretched})$, avoiding overcooling of the human body. However, for a chest skin temperature of 309 K (close to the mean temperature of the human body), the heat fluxes can be positive, i.e. heat into the skin, or negative, i.e. heat drawn from the skin (with P_{net} = 79.1 Wm⁻² when relaxed and P_{net} = -62.5 Wm⁻² when stretched).

The mismatch between the measured and modelled heat flux could be explained by the imperfect contact between the skin and the samples. If we assume a thermal contact resistance of 6.25×10^{-3} Km²W⁻¹, which is taken from previous experimental results on human skin [64], we notice a reduction in the heat flux. For the chest, the heat flux at the fully relaxed state with the thermal contact resistance is estimated to be 56 Wm⁻² into the skin (112 Wm⁻² without the resistance). For the wrist under similar conditions, the heat flux is estimated to be 160 Wm⁻² (320 Wm⁻² without the resistance).

The use of the corrugated nickel samples on the human skin, however, would impede the natural evapotranspiration cooling provided by sweating. We thus compare the heat loss due to potential evapotranspiration with the neat heat loss to the stretched corrugated nickel samples. The evaporative heat loss from the skin can be given as $P_{evap} = S \cdot h_v$, with S being the sweat rate and h_v being the latent heat of evaporation $(2.427 \times 106 \text{ Jkg}^{-1})$ [65]. The sweat rate for the human body is estimated to be $1.667 \times 10^{-5} - 8.333 \times 10^{-5} \text{ kgs}^{-1}\text{m}^{-2}$ (for a skin temperature varying between 308–314 K) [65]. This results in an evaporative heat loss of 40-202 Wm⁻² for the human skin [65,66]. The stretched corrugated nickel samples on the chest can provide comparable cooling of 62 Wm⁻² and enables dynamic control at will, which is enabled by simple mechanical strain.

The device durability could be affected by temperature, humidity, and sweat on the human body where it's placed. To analyze the life of the elastomer substrate, we compute the number of cycles the elastomer would be able to resist before breaking. The acrylic substrate used in this work has shown excellent fatigue life in previous research, where stretchable electrodes based on wrinkled elastomers were fabricated and tested after 100,000 cycles, showing little effect in the performance of the device [67]. Evaluating the fatigue response for the samples by using the data obtained in past studies, where the crack growth rate was measured during a cyclic loadingunloading test [68], we estimate that the samples can withstand up to 10^7 cycles before breaking, even assuming the pre-existence of a 0.18 mm crack present in the elastomeric substrate, with the value dramatically increasing for smaller initial cracks. This estimation is performed considering the substrate undergoes a strain of 200%.

Discussions

Recent studies of radiative cooling and heating have presented various designs of selective emitters. The results obtained in this study extend the application of selective emitters with the use of dynamically tunable control. While existing selective emitters consist of largely rigid structures offering static emissivity profiles, the integration of the corrugated nickel with the elastomer substrate enhances the dynamic tuning of emissivity and optical properties with simple mechanical straining. The corrugated nickel-based selective emitters presented here follow simple fabrication techniques based on the integration of metal deposition on a pre-strained stretchable elastomer substrate. The resultant structures offer emissivity control over the solar spectrum with values ranging from 0.3 to 0.7 based on varying levels of stretching.

Considering the natural variability of ambient climatic conditions, where thermal boundary conditions can have a big impact on the heating and cooling rates of the human body, the controlled control of radiative and thermal properties by a simple mechanical actuation is a significant improvement to the state-of-the-art. The simple stretching and relaxation pose



a considerable advantage over other methods of emissivity control, such as PCMs with their transition temperature-limited applications.

The dynamic control of optical properties can be applied to systems and surfaces where a quickly tunable spectral and thermal response is desired. The 10–12 K control in temperature allows the device to perform within a wide range of solar and ambient conditions, while maintaining a controlled surface temperature. The structure-induced thermal control offers solutions suited for various applications ranging from comfort clothing to smart windows and wearable electronic devices.

The samples presented here have been tested in Irvine, California during the summer, where the average solar irradiance is 1947 kWhm⁻² per year, and the ambient air temperature varies from 286 K to 300 K. These ambient values are similar to a vast majority of highly populated regions in the world, as in South America, Africa, India and Australia. In these regions, our design is rendered feasible to be applied to human body thermal management. The fabricated product is tested to be wearable on the chest and wrist, where it maintains its functionality, acting as a proof-of-concept for its use in personal thermal management systems. In the case of use on the chest, the product can deliver a positive or negative net heat flux to the skin below, making both heating or cooling possible in the typical range of human body temperature (308–314 K), by means of stretching or releasing the substrate. When a hypothermic state is reached (308 K), the structure provides net heating to the skin, similarly providing net cooling to the skin in the opposite case, when the body is in a hyperpyrexia condition at 314 K.

In different ambient environmental conditions, especially colder parts of the world, such as Canada, northern Europe or Russia, the corrugated nickel performs less than ideally as a personal thermal regulator. However, it can have other equally interesting applications such as thermoregulation of devices around the ambient air temperature (Figure S9). Further evaluation of the corrugated metallic selective emitters for radiative cooling would increase the applicability of the samples towards varying geographic, climatic, and system-level demands.

Conclusions

While conventional radiative thermal management solutions are based on passive selective emitters, the presented results offer dynamic emissivity control based on a bio-inspired design using a corrugated nickel-based stretchable emitter. The emissivity varies from 0.7 to 0.3 in the visible spectrum, by means of mechanical stretching and relaxation of the elastomeric substrate. The variations in the emissivity are tested over 20 cycles of stretching and relaxation to ensure reliability and endurance, and show negligible deterioration in the emissivity of the corrugated and stretched nickel through the cycling.

The strain-induced emissivity variations result in changes in the surface temperature of the corrugated nickel. While the corrugated nickel of 700 nm pitch exhibits a surface temperature of 310–315 K at daytime ambient conditions, the stretched nickel (and flat nickel) exhibits temperatures of 303–306 K. With the tunable surface temperature in the range of 303–315 K and with the human body temperature at an average of 305–309 K, we tested the use of corrugated nickel-based selective emitters for personal thermal management. When placed at the chest, the corrugated samples are estimated to provide 79.2 Wm $^{-2}$ of heat into the human body, and the stretched samples draw 62.5 Wm $^{-2}$ of heat out of the body . When placed at the wrist, the corrugated samples are estimated as P_{net} of 1.4 Wm $^{-2}$ of heat going into the skin while stretched and 142.9 Wm $^{-2}$ of heat going into the skin while relaxed.

The large changes in heat flux are enabled by the application of simple mechanical strain, and can also be facilitated by flexion or extension of various locations across the human body, such as on the wrist. These findings advance our understanding of relationships between topography, emissivity, and temperature and enable breakthroughs in dynamic thermal control on flexible and wearable systems.



Methods

Fabrication of corrugated nickel samples

To fabricate the corrugated nickel samples, we deposit a 10 nm nickel film on a pre-strained 25 mm by 25 mm elastomer substrate using electron beam deposition (Temescal CV-8). By carefully tuning the electron gun power, we control the chamber temperature to avoid any thermal damage to the elastomer and a low deposition rate (less than 0.5 Å/s) to ensure the film uniformity. The corrugation pitch is dependent on the film thickness and the mechanical proper-

ties as follows:
$$Pitch = \frac{2\pi h_f}{\left(1+\varepsilon_{pre}\right)(1+\xi)^{1/3}} \left[\frac{E_f\left(1-v_s^2\right)}{3E_s\left(1-v_f^2\right)}\right]^{1/3}$$
, where $\xi = \frac{5}{32}\varepsilon_{pre}\left(1+\varepsilon_{pre}\right)$ [69]. Here, the

Young's modulus is given by E, and the Poisson's ratio is given by ν , with the subscripts f denoting the metallic layer, and s denoting the substrate. The pre-strain value is denoted as ε_{pre} , while the deposited layer thickness is given by h_f . In order to achieve a pitch of around 700 nm, the required nickel layer thickness is estimated to be 10 nm. We manually stretched the substrates to a pre-strain value of 250% and taped them in place onto the evaporator's sample holder. After depositing nickel onto the stretched substrate, we slowly released the pre-strain to induce corrugation, and a corrugation pitch of 600-800 nm was formed as verified by SEM imaging (Figure S3).

Measurement of optical properties

The optical properties of corrugated and flat nickel are characterized by using commercial spectrometers, the Cary 7000 Universal Measurement Spectrometer (UMS) and the Jasco V-670, with a 60 mm integrating sphere. The measurements were calibrated against a standard white body, and the reflectivity and transmissivity spectra were compared with theoretical models, validating the experimental capabilities of the optical system. The emissivity is then calculated based on the sum of the reflectivity, transmissivity, and emissivity being unity. The spectrometer is used to verify the corrugation-dependent emissivity changes in the spectral range of 0.2 to 2.5 µm. The experimental setup and the computation model were also separately calibrated with control samples including a bare silicon substrate and silicon nanowire arrays. The inherent uncertainty in the optical properties is ± 0.003 for the properties ranging from 0 to 1, with the wavelength uncertainty during measurement being ±0.3 nm at a stable room temperature of 293 K.

Temperature measurement

We performed the temperature measurement for the corrugated nickel system by itself, and on top of human skin. We placed the stretcher device on a petri dish attached to three thermal isolation legs, to reduce thermal losses due to conduction. We measured the temperature on top of the surface using a thermocouple. We conducted one experiment in normal wind conditions, and one experiment using a polyethylene film to reduce the convection effects (Supplementary **Information Section S7**). The resolution of the thermocouples is 0.1 K with an inherent uncertainty of ±1.1 K at a measurement range of 273-328 K.

For the on-skin measurement, we used an IR camera (FLIR A655sc) that was first properly calibrated with the IR emissivity of the samples. The substrate was placed on top of the wrist (at 305 K), attached to the skin and secured using black tape to ensure the flexing motion of the wrist stretched the sample in a controlled manner. We allowed for the temperature to reach a steady state condition and recorded the value from the camera. The resolution of the IR camera is 0.03 K with an inherent uncertainty of ±0.5 K for a measurement range of 273-343 K. The temperature values recorded for any surface by the IR camera is measured as



an average of the temperatures of the pixels within the measured surface. The uncertainty in measurement recorded for the measurement is given as $\pm \sigma$, where σ denotes one standard deviation from the mean.

The measurements from the IR camera and thermocouple were compared while recording the surface temperature of a standard black surface (3M Super88 tape, with an IR emissivity of 0.96) under an ambient convective heat transfer coefficient of $12~{\rm Wm^{-2}K^{-1}}$ and an air temperature of 300 K. While the IR camera recorded a mean temperature of 318.8 K, the thermocouple recorded a temperature of 319.1 K. Under the same ambient atmospheric conditions, the corrugated nickel sample recorded a surface temperature of 312.6 K with the IR camera and 314 K with the thermocouple. Meanwhile, the flat nickel recorded a surface temperature of 306 K with the IR camera and with the thermocouple.

Acknowledgments

J.L. thanks the support from the Henry Samueli School of Engineering at the University of California at Irvine and the Hellman Faculty Award, M.S-C. thanks the Balsells Fellowship, and A.K. thanks the Henry Samueli School of Engineering Ph.D. Bridge Fellowship. SEM and AFM were performed at the UC Irvine Materials Research Institute (IMRI), and the authors thank Dr. Q. Lin for the training and assistance provided. The metal deposition was performed at the UC Irvine Integrated Nanosystems Research Facility (INRF). The optical properties were measured at the Laser Spectroscopy Labs (LSL) at UC Irvine, and the authors thank Dr. D. Fishman for the training and assistance provided. The authors acknowledge Dr. Sungwoo Nam's intellectual contributions on surface corrugation control and Dr. Alon Gorodetsky's intellectual contributions on wearable thermoregulation.

Author contributions

J.L. conceived the idea and supervised the research. M.S-C. performed the thermal and RCWA computations, SEM imaging and obtained temperature data. A.K. performed the optical properties measurements, SEM imaging, AFM analysis, FDTD computations, and the on-skin heat flux experiments. Z.Y. performed the fabrication of the samples. M.S-C., A.K., and J.L. wrote the paper. All authors commented on the manuscript.

Competing financial interests

The authors declare no competing financial interests.

ORCID

Martí Sala-Casanovas (b) http://orcid.org/0000-0001-8941-3888 Anirudh Krishna (b) http://orcid.org/0000-0002-5619-1569 Ziqi Yu (b) http://orcid.org/0000-0001-6740-6433 Jaeho Lee (b) http://orcid.org/0000-0002-2207-4399

References

- [1] P. D. García, R. Sapienza, Á. Blanco, and C. López, "Photonic glass: a novel random material for light," *Adv Mater*, vol. 19, no. 18, pp.2597–2602, 2007. DOI: 10.1002/(ISSN)1521-4095.
- [2] L. De Sio, N. Tabiryan, T. Bunning, B. R. Kimball, and C. Umeton, "Dynamic photonic materials based on liquid crystals," *Prog Opt*, vol. 58, pp. 1–64, 2013.
- [3] Y. J. Liu, Z. Cai, E. S. P. Leong, X. S. Zhao, and J. H. Teng. "Optically switchable photonic crystals based on inverse opals partially infiltrated by photoresponsive liquid crystals," *J Mater Chem*, vol. 22, no. 15, pp. 7609–7613, 2012. DOI:10.1039/c2jm16050a
- [4] E. Vargo, "Finding nanostructures that reproduce colors with adaptive mesh search techniques," *J Opt Soc Am B*, vol. 34, no. 10, pp. 2250, Oct. 2017. DOI: 10.1364/JOSAB.34.002250.
- [5] Y. Fu, C. A. Tippets, E. U. Donev, and R. Lopez, "Structural colors: from natural to artificial systems," Wiley Interdiscip Rev Nanomed Nanobiotechnol, vol. 8, no. 5, pp. 758–775, Sep. 2016. DOI: 10.1002/wnan.1396.



- [6] J. Teyssier, S. V. V. Saenko, D. van der Marel, and M. C. C. Milinkovitch, "Photonic crystals cause active colour change in chameleons," Nat Commun, vol. 6, no. 1, pp. 6368, Dec. 2015. DOI: 10.1038/ncomms7368.
- [7] K. M. Cooper, R. T. Hanlon, and B. U. Budelmann, "Physiological color change in squid iridophores," Cell Tissue Res, vol. 259, no. 1, pp. 15-24, Jan. 1990. DOI: 10.1007/BF00571425.
- [8] C. M. Osborn, "The physiology of color change in flatfishes," J Exp Zool, vol. 81, no. 3, pp. 479–515, Aug. 1939. DOI: 10.1002/(ISSN)1097-010X.
- [9] F. Liu, B. Q. Dong, X. H. Liu, Y. M. Zheng, and J. Zi, "Structural color change in longhorn beetles Tmesisternus isabellae," Opt Express, vol. 17, no. 18, pp. 16183-16191, Aug. 2009. DOI: 10.1364/OE.17.016183.
- [10] B. K. Hsiung, et al. "Rainbow peacock spiders inspire miniature super-iridescent optics," Nat Commun, vol. 8, no. 1, 2278.Dec. 2017. DOI: 10.1038/s41467-017-02451-x.
- [11] W. Zhang, G. Xu, J. Zhang, H. Wang, and H. Hou, "Infrared spectrally selective low emissivity from Ge/ZnS one-dimensional heterostructure photonic crystal," Opt Mater (Amst), vol. 37, no. C, pp. 343-346, Nov. 2014. DOI: 10.1016/j.optmat.2014.06.023.
- [12] S. Schauer, J. J. Baumberg, H. Hölscher, and S. K. Smoukov, "Tuning of structural colors like a chameleon enabled by shape-memory polymers", Macromol Rapid Commun, p. 1800518, Sep 2018.
- [13] H. Butt, et al., "Morpho butterfly-inspired nanostructures," Adv Opt Mater, vol. 4, no. 4, pp. 497–504, Apr. 2016. DOI: 10.1002/adom.201500658.
- [14] D. Stuart-Fox and A. Moussalli, "Selection for social signalling drives the evolution of chameleon colour change," PLoS Biol, vol. 6, no. 1, pp. e25, Jan. 2008. DOI: 10.1371/journal.pbio.0060098.
- [15] N. N. Shi, et al., "Keeping cool: enhanced optical reflection and radiative heat dissipation in Saharan silver ants.," Science, vol. 349, no. 6245, pp. 298-301, Jul. 2015. DOI: 10.1126/science.aab3564.
- [16] C. A. Gueymard, D. Myers, and K. Emery, "Proposed reference irradiance spectra for solar energy systems testing," Sol Energy, vol. 73, no. 6, pp.443-467, 2002. DOI: 10.1016/S0038-092X(03)00005-7.
- [17] L. Cai, et al. "Warming up human body by nanoporous metallized polyethylene textile," Nat Commun, vol. 8, no. 1, pp. 496, 2017. DOI: 10.1038/s41467-017-00614-4.
- S. D. Lord. "A new software tool for computing earth's atmospheric transmission of near-and far-infrared radiation," NASA Technical Memorandum 103957, 1992.
- [19] S. Catalanotti, et al., "The radiative cooling of selective surfaces," Sol Energy, vol. 17, no. 2, pp.83–89, 1975. DOI: 10.1016/0038-092X(75)90062-6.
- [20] A. P. Raman, M. A. Anoma, L. Zhu, E. Rephaeli, and S. Fan, "Passive radiative cooling below ambient air temperature under direct sunlight," Nature, vol. 515, no. 7528, pp.540-544, 2014. DOI: 10.1038/nature13883.
- [21] J. Long Kou, Z. Jurado, Z. Chen, S. Fan, and A. J. Minnich, "Daytime radiative cooling using near-black infrared emitters," ACS Photonics, vol. 4, no. 3, pp.626-630, 2017. DOI: 10.1021/acsphotonics.6b00991.
- [22] Y. Zhai, et al. "Scalable-manufactured randomized glass-polymer hybrid metamaterial for daytime radiative cooling,," Science, vol. 355, no. 6329, 1062-1066, Feb. 2017. DOI: 10.1126/science.aai7899.
- [23] A. Krishna and J. Lee, "Morphology-driven emissivity of microscale tree-like structures for radiative thermal management," Nanoscale Microscale Thermophys Eng, vol. 22, no. 2, pp. 124-136, Apr. 2018. DOI: 10.1080/ 15567265.2018.1446065.
- [24] Y. M. Song, J. S. Yu, and Y. T. Lee, "Antireflective submicrometer gratings on thin-film silicon solar cells for light-absorption enhancement.," Opt Lett, vol. 35, no. 3, pp. 276–278, Feb. 2010. DOI: 10.1364/OL.35.000276.
- [25] W. Ma, Y. Wen, and X. Yu, "Broadband metamaterial absorber at mid-infrared using multiplexed cross resonators," Opt Express, vol. 21, no. 25, pp. 30724-30730, Dec. 2013. DOI: 10.1364/OE.21.017108.
- [26] T. Maier and H. Brückl, "Wavelength-tunable microbolometers with metamaterial absorbers," Opt Lett, vol. 34, no. 19, pp. 3012-3014, Oct. 2009. DOI: 10.1364/OL.34.003012.
- [27] P. C. Hsu, et al. "Personal thermal management by metallic nanowire-coated textile," Nano Lett, vol. 15, no. 1, pp. 365-371, 2015. DOI: 10.1021/nl504066f.
- [28] R. Osiander, S. L. Firebaugh, J. L. Champion, D. Farrar, and M. A. G. Darrin, "Microelectromechanical devices for satellite thermal control," IEEE Sens J, vol. 4, no. 4, pp.525-531, 2004. DOI: 10.1109/JSEN.2004.830297.
- [29] P.-C. Hsu, et al. "A dual-mode textile for human body radiative heating and cooling," Sci Adv, vol. 3, no. 11, e1700895.Nov. 2017. DOI: 10.1126/sciadv.1700895.
- [30] D.-H. Kim and J. A. Rogers, "Stretchable electronics: materials strategies and devices," Adv Mater, vol. 20, no. 24, pp. 4887–4892, Dec. 2008. DOI: 10.1002/adma.v20:24.
- [31] A. M. Hussain, et al., "Metal/polymer based stretchable antenna for constant frequency far-field communication in wearable electronics," Adv Funct Mater, vol. 25, no. 42, pp. 6565-6575, Nov. 2015. DOI: 10.1002/ adfm.201503277.
- [32] C. Yan, et al. "Stretchable and wearable electrochromic devices," ACS Nano, vol. 8, no. 1, 316-322.Jan. 2014. DOI: 10.1021/nn404061g.
- [33] Y. Peng, et al. "Nanoporous polyethylene microfibres for large-scale radiative cooling fabric," Nat Sustain, vol. 1, no. 2, 105-112.Feb. 2018. DOI: 10.1038/s41893-018-0023-2.



- [34] P. B. Catrysse, A. Y. Song, and S. Fan, "Photonic structure textile design for localized thermal cooling based on a fiber blending scheme," ACS Photonics, vol. 3, no. 12, pp. 2420-2426, Dec. 2016. DOI: 10.1021/ acsphotonics.6b00644.
- [35] J. K. Tong, et al., "Infrared-transparent visible-opaque fabrics for wearable personal thermal management," ACS Photonics, vol. 2, no. 6, pp. 769-778, Jun. 2015. DOI: 10.1021/acsphotonics.5b00140.
- [36] L. Cai, et al. "Spectrally selective nanocomposite textile for outdoor personal cooling," Adv Mater, vol. 30, no. 35, 1802152.Aug. 2018. DOI: 10.1002/adma.201802152.
- [37] Z. Chen, L. Zhu, A. Raman, and S. Fan, "Radiative cooling to deep sub-freezing temperatures through a 24-h day-night cycle," Nat Commun, vol. 7, pp. 13729, 2016. DOI: 10.1038/ncomms13729.
- [38] S. Taylor, Y. Yang, and L. Wang, "Vanadium dioxide based Fabry-Perot emitter for dynamic radiative cooling applications," J Quant Spectrosc Radiat Transf, vol. 197, pp. 76-83, 2017. DOI: 10.1016/j.jqsrt.2017.01.014.
- [39] -K.-K. Du, et al. "Control over emissivity of zero-static-power thermal emitters based on phase-changing material GST," Light Sci Appl, vol. 6, no. 1, pp. e16194, 2017. DOI: 10.1038/lsa.2016.194.
- [40] X. Liu, et al., "Taming the blackbody with infrared metamaterials as selective thermal emitters," Phys Rev Lett, vol. 107, no. 4, pp. 045901, Jul. 2011. DOI: 10.1103/PhysRevLett.107.045901.
- [41] A. Narayanaswamy and G. Chen, "Thermal emission control with one-dimensional metallodielectric photonic crystals," Phys Rev B, vol. 70, no. 12, pp. 125101, Sep. 2004. DOI: 10.1103/PhysRevB.70.125101.
- [42] R. A. Lowe, D. L. Chubb, S. C. Farmer, and B. S. Good, "Rare-earth garnet selective emitter," Appl Phys Lett, vol. 64, no. 26, pp. 3551–3553, Jun. 1994. DOI: 10.1063/1.111221.
- [43] W. Sabuga and R. Todtenhaupt, "Effect of roughness on the emissivity of the precious metals silver, gold, palladium, platinum, rhodium, and iridium," High Temp - High Press, vol. 33, no. 3, pp.261-269, 2001. DOI: 10.1068/htwu371.
- [44] A. G. Worthing, "Physical properties of well seasoned molybdenum and tantalum as a function of temperature," Phys Rev, vol. 28, no. 1, pp.190-201, 1926. DOI: 10.1103/PhysRev.28.190.
- [45] B. Jae Lee, Y.-B. Chen, S. Han, F.-C. Chiu, and H. Jin Lee, "Wavelength-selective solar thermal absorber with two-dimensional nickel gratings," J Heat Transfer, vol. 136, no. 7, pp.072702, 2014. DOI: 10.1115/1.4026954.
- [46] S. Zeng, et al. "Bio-inspired sensitive and reversible mechanochromisms via strain-dependent cracks and folds," Nat Commun, vol. 7, pp. 11802. Jul. 2016. DOI:10.1038/ncomms11802.
- [47] S. G. Lee, et al., "Switchable transparency and wetting of elastomeric smart windows," Adv Mater, vol. 22, no. 44, pp. 5013-5017, Nov. 2010. DOI: 10.1002/adma.v22.44.
- [48] E. Lee, et al. "Tilted pillars on wrinkled elastomers as a reversibly tunable optical window," Adv Mater, vol. 26, no. 24, 4127-4133.Jun. 2014. DOI: 10.1002/adma.201402404.
- [49] C. Xu, G. T. Stiubianu, and A. A. Gorodetsky, "Adaptive infrared-reflecting systems inspired by cephalopods," Science, vol. 359, no. 6383, pp.1495–1500, 2018. DOI: 10.1126/science.aar5191.
- [50] S. Peng and G. M. M. Morris, "Efficient implementation of rigorous coupled-wave analysis for surface-relief gratings," J Opt Soc Am A, vol. 12, no. 5, pp.1087-1096, 1995. DOI: 10.1364/JOSAA.12.001087.
- [51] M. G. Moharam and T. K. Gaylord, "Rigorous coupled-wave analysis of planar-grating diffraction," J Opt Soc Am, vol. 71, no. 7, pp.811–818, 1981. DOI: 10.1364/JOSA.71.000811.
- [52] A. Taflove and S. C. Hagness, Computational Electrodynamics, the Finite-Difference Time-Domain Method. Norwood, MA: Artech House. 2005.
- [53] Y. Huang, Q. Zhao, S. K. Kalyoncu, R. Torun, and O. Boyraz, "Silicon-on-sapphire mid-IR wavefront engineering by using subwavelength grating metasurfaces," J Opt Soc Am B, vol. 33, no. 2, pp.189-194, 2016. DOI: 10.1364/JOSAB.33.000189.
- [54] J. R. Howell, M. P. Menguc, and R. Siegel, Thermal Radiation Heat Transfer. Boca Raton, FL: CRC Press. 2016.
- [55] M. A. Ordal, R. J. Bell, R. W. Alexander, L. L. Long, and M. R. Querry, "Optical properties of fourteen metals in the infrared and far infrared: Al, Co, Cu, Au, Fe, Pb, Mo, Ni, Pd, Pt, Ag, Ti, V, and W," Appl Opt, vol. 24, pp. 4493, 1985.
- [56] M. A. Ordal, R. J. Bell, R. W. Alexander, L. L. Long, and M. R. Querry, "Optical properties of Au, Ni, and Pb at submillimeter wavelengths," Appl Opt, vol. 26, no. 4, pp.744, 1987. DOI: 10.1364/AO.26.003940.
- [57] E. D. Palik, Handbook of Optical Constants of Solids, Vol. 1, San Diego, CA: Academic Press. 2012.
- [58] S. Shian and D. R. Clarke, "Electrically tunable window device," Opt Lett, vol. 41, no. 6, pp.1289, 2016. DOI: 10.1364/OL.41.004919.
- M. Shrestha and G.-K. Lau, "Tunable window device based on micro-wrinkling of nanometric zinc-oxide thin film on elastomer," Opt Lett, vol. 41, no. 19, pp.4433, 2016. DOI: 10.1364/OL.41.004919.
- [60] "3M, "VHB TM tapes technical data"", St. Paul, MN: 3M Industrial Adhesives and Tapes Division. November
- [61] E. M. Sparrow and S. H. Lin, "Absorption of thermal radiation in a V-groove cavity," Int J Heat Mass Transf, vol. 5, no. 11, pp.1111–1115, 1962. DOI: 10.1016/0017-9310(62)90064-9.
- [62] J.-H. Choi and V. Loftness, "Investigation of human body skin temperatures as a bio-signal to indicate overall thermal sensations," Build Environ., vol. 58, pp. 258-269, Dec 2012. DOI: 10.1016/j.buildenv.2012.07.003.



- [63] N. Romeijn and E. J. W. Van Someren, "Correlated fluctuations of daytime skin temperature and vigilance," J Biol Rhythms, vol. 26, no. 1, pp. 68–77, Feb. 2011. DOI: 10.1177/0748730410391894.
- [64] B. Saggin, M. Tarabini, and G. Lanfranchi, "A device for the skin-contact thermal resistance measurement," *IEEE Trans Instrum Meas*, vol. 61, no. 2, pp.489–495, 2012. DOI: 10.1109/TIM.2011.2169179.
- [65] T. V. McCaffrey, R. D. Wurster, H. K. Jacobs, D. E. Euler, and G. S. Geis, "Role of skin temperature in the control of sweating," J Appl Physiol, vol. 47, no. 3, pp.591–597, 1979. DOI: 10.1152/jappl.1979.47.3.591.
- [66] D. Gagnon, O. Jay, and G. P. Kenny, "The evaporative requirement for heat balance determines whole-body sweat rate during exercise under conditions permitting full evaporation," *J Physiol*, vol. 591, no. 11, pp.2925— 2935, 2013. DOI: 10.1113/jphysiol.2012.247577.
- [67] G.-B. Lee, S. G. Sathi, D.-Y. Kim, K.-U. Jeong, and C. Nah, "Wrinkled elastomers for the highly stretchable electrodes with excellent fatigue resistances," *Polym Test.*, vol. 53, pp. 329–337, Aug 2016. DOI: 10.1016/j. polymertesting.2016.06.003.
- [68] W. Fan, Y. Wang, and S. Cai, "Fatigue fracture of a highly stretchable acrylic elastomer," *Polym Test.*, vol. 61, pp. 373–377, Aug 2017. DOI: 10.1016/j.polymertesting.2017.06.005.
- [69] C. Yu and H. Jiang, "Forming wrinkled stiff films on polymeric substrates at room temperature for stretchable interconnects applications," *Thin Solid Films*, vol. 519, no. 2, pp.818–822, 2010. DOI: 10.1016/j.tsf.2010.08.106.